In-situ graphene doping as a route towards efficient perovskite tandem solar cells

Felix Lang*, Marc A. Gluba*, Steve Albrecht, Oleksandra Shargaieva, Jörg Rappich, Lars Korte, Bernd Rech, and Norbert H. Nickel

Helmholtz-Zentrum Berlin für Materialien und Energie GmbH, Institut für Silizium Photovoltaik, Kekuléstr. 5, 12489 Berlin, Germany.

Received ZZZ, revised ZZZ, accepted ZZZ
Published online ZZZ (Dates will be provided by the publisher.)

Keywords Perovskite, transparent contact, graphene, spiro-OMeTAD

* Corresponding author: e-mail felix.lang@helmholtz-berlin.de, Phone: +00 49 30 8062 41354, Fax: +00 49 30 8062 41333
* Corresponding author: e-mail marc.gluba@helmholtz-berlin.de, Phone: +00 49 30 8062 41314, Fax: +00 49 30 8062 41333

Tandem solar cells consisting of perovskite and silicon absorbers have the potential to outperform respective state-of-the-art single junction efficiencies. However, their development requires the gentle deposition of a transparent electrode onto the hybrid perovskite and its organic layers. Implementation of large area graphene obtained by chemical vapour deposition seems to be an excellent solution. In this manuscript we present the impact of graphene on perovskite solar cells and their organic layers. Direct application of graphene on $CH_3NH_3PbI_3$ is limited by a highly defective interface but insertion of spiro-OMeTAD enables a defect free implementation. Solar cells containing transparent graphene contacts approach identical electrical performance compared to devices with standard Au contacts. Hall-effect measurements of graphene on various organic thin-films, revealed the importance of field effect doping. Gained knowledge enabled the development of a strategy to increase the charge carrier density in graphene by 60 %, while lowering graphene sheet resistance by 24 %. This combined route of spiro-OMeTAD and stabilized adsorbent doping is an important step towards the targeted application in high performance monolithic perovskite/silicon tandem solar cells.

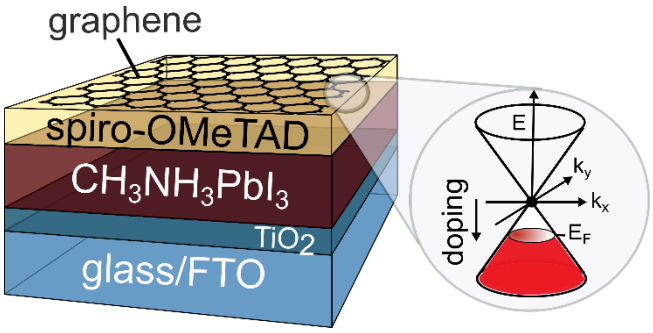

.

1 Introduction Semiconducting organic-inorganic perovskites, e.g.: $CH_3NH_3PbI_3$, combine outreaching optoelectronic properties such as high absorption coefficients [1], low exciton binding energy [2], high diffusion lengths [3] and low recombination rates [4,5]. At the same time fundamental properties such as the band-gap energy can easily be tuned by cation [6] or halide [7] exchange. Today, power conversion efficiencies in perovskite single junctions exceed 20 % [8]. Very important is the low sub-band-gap absorption and the high band gap energies of 1.57 eV for $CH_3NH_3PbI_3$ [9]. This is advantageous for the combination with silicon (Si) or copper indium gallium diselenide (CIGS) absorbers in tandem solar cells. The combination of a high and low band gap absorber allows reducing thermalization losses. Hence, power conversion efficiencies beyond respective single junction limits are anticipated. Recently, record efficiencies of 28 % have been reported using the simplest implementation of fully optimized perovskite (15 %) and Si solar cells (25 %) with a dichroic beam-splitter [10].

A realistic application, however, requires the deposition of a transparent electrode onto the hybrid perovskite and its organic layers. Contacting a tandem solar cell, this electrode must be highly transparent in the visible and near-IR regime. Recently, we claimed large-area graphene to be an optimal solution to tackle this challenge [11]. On the other hand, straight forward implementation of indium doped tin oxides (ITO) on 2,2',7,7'-tetrakis-(N,N-di-4-methoxyphenylamino)-9,9'-spirobifluorene (spiro-OMeTAD) by sputtering deteriorates the topmost hole

transport layer. Therefore, efficient tandem solar cells require minimization of the sputter damage. This is typically achieved by either inserting thin buffer layers of thermally evaporated MoO_x [12,13] or elaborate optimization of applied sputter procedures and materials [14,15]. By these means power conversion efficiencies exceeding 18 % have been reported in monolithic [13] and 4-terminal tandem solar cells [14]. Despite achieved efficiencies the open circuit voltage is still significantly reduced by tens to hundreds of mV.[12,13]

While sputtered electrodes are additionally limited by processability electrodes based on large area graphene are fully compatible to solution processing as well as to the perovskite and its organic hole conductors. Especially roll-to-roll processing of graphene electrodes on perovskite solar cells holds a great promise for the future. It has been shown that implementation of graphene in perovskite solar cells allows the preparation of efficient 4-terminal tandem solar cells with initial efficiencies of 13.2 % [11]. This achievement was enabled by the low absorption of graphene of about 2.3 %, extending from 500 nm to the mid IR regime, as shown in [16]. Therefore, the defect free implementation with negligible loss in open circuit voltage [11,17] renders this solution attractive for future high efficiency tandem solar-cells for monolithic and 4-terminal geometries.[11] At the moment moderate graphene sheet resistance can hamper FF and device performance.

In this paper, we show a twofold approach to overcome this limitation. First, we identified fundamental implications of typical organic hole conductors on the properties of graphene. Understanding of these mutual influences will allow an in-situ doping of the transferred graphene layers. The increase in the charge carrier density is needed to lower the sheet resistance. Second, we calculate a realistic perspective by combining graphene with generous spaced metal grids. Combining both will be a first step towards efficient graphene contacted perovskite/Si tandem solar cells.

For this purpose large area graphene was grown by chemical vapour deposition (CVD) on copper foil [18,19] and transferred onto various substrates. The influence of the underlying layers – glass, spiro-OMeTAD or PEDOT:PSS – on the charge carrier mobility and concentration in the graphene monolayer was studied using Hall-effect measurements. It is important to note that the observed doping and interface defects can have tremendous influence on solar cell performance. Therefore, planar perovskite solar cells with graphene and Au contacts were fabricated following the well-established layer sequence glass/FTO/TiO_2/$CH_3NH_3PbI_3$ – with and without spiro-OMeTAD, as depicted in figure 1. In contrast to other reports [17] large area graphene layers are implemented on the perovskite solar cell following a wet transfer, without the need of additional PEDOT:PSS layers. This renders the device structure less complex and more transparent.

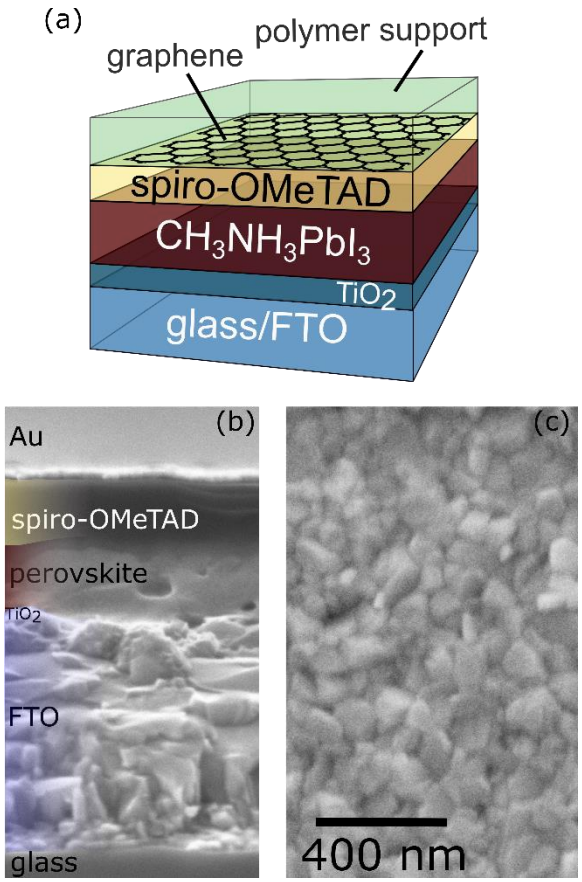

Figure 1 (a) Schematic drawing of the perovskite solar cell with transparent large area CVD-graphene contact. (b) Cross sectional SEM image of a typical perovskite solar cell consisting of the layer stack glass/FTO/TiO_2/$CH_3NH_3PbI_3$/spiro-OMeTAD/Au. (c) Top view SEM image of the perovskite absorber on glass/FTO/TiO_2.

2 Experimental

2.1 Preparation of large area graphene Graphene sheets were grown on a scale of several tens of square centimetres by using the catalytic decomposition of methane on copper in a hot wall CVD process. After precleaning in acetone, isopropanol and acetic acid, the 25 µm thick Cu foil (99.999 % purity) was heated in hydrogen atmosphere to 1000°C to remove residual surface oxygen and enlarge the Cu grain size. In a second step a flow of 11.4 sccm of methane was introduced into the furnace and graphene growth was conducted for 60 minutes.

2.1 Preparation of graphene on organic layers Prepared large area graphene sheets were transferred onto various substrates for electrical and optical characterization. Therefore, cleaned glass substrates were either used as is, or coated with poly(3,4-ethylenedioxythiophene) polystyrene sulfonate (PEDOT:PSS, Heraeus PH4083) and spiro-OMeTAD. The polymer layers were obtained by spin coat-

ing at 3000 rpm for 30 s followed by heating at 180°C for 10 minutes, while the latter is spin coated at 2000 rpm for 30 s. The graphene was cut into 1 cm^2 pieces and subsequently coated with a polymer support layer. Finally, the copper foil was etched off using concentrated $FeCl_3$ solution. Prior to the transfer step the obtained free standing graphene/support films were washed with pure H_2O. Transfer of the freestanding graphene/support films is performed following a wet transfer.[19] In case of sensitive organic and perovskite layers anhydrous solvents were used instead of H_2O.

2.3 Perovskite solar cell fabrication Planar perovskite solar cells were prepared on FTO coated glass (Solaronix, R = 8 Ω/sq). Prior to the deposition the substrates were cleaned in ultrasonic baths using detergent/H_2O, acetone and isopropanol. Subsequently, a thin compact TiO_2 layer was grown by spray pyrolysis from titanium diisopropoxide bis(acetylacetonate) (Sigma) at 450°C in nitrogen atmosphere. Prior to the perovskite deposition the glass/FTO/TiO_2 substrates were calcined at 450°C for 30 min in air. $CH_3NH_3PbI_3$ was prepared by spin-coating from a stoichiometric precursor solution following a previously published routine in nitrogen atmosphere [6]. The precursor solution contained 0.8 M PbI_2 (99.8 %, Sigma) and CH_3NH_3I (synthesized from HI and CH_3NH_2, Sigma) [20] in γ-butryolactone and dimethyl sulfoxide (70 vol % / 30 vol %). After crystallisation at 100°C for 10 min the perovskite layer had a thickness of around 280 nm. Unless otherwise stated, the solar cell was completed by depositing the hole-conductor spiro-OMeTAD (Merck). Therefore, spiro-OMeTAD was dissolved in chlorobenzene (80 mg/ml) and spin-coated at 2000 rpm for 30 s. The used spin coating formulation contained 8.5 µl of a stock solution of bis (trifluoromethane) sulfonimide lithium salt (LiTFSI, Lumtec, 170 mg/ml in acetonitrile) and 46.4 µl 4-tert-butylpyridine (TBP, Sigma). Finally, the electrodes were deposited by either thermal evaporation of 80 nm Au (10^{-7} mbar, 0.7 Å/s) or by incorporating large area graphene.

2.2 Characterization Raman spectra were acquired at room temperature in backscattering geometry using the 488 nm emission of an Ar^+ ion laser. The spectral resolution was better than 0.5 cm^{-1}. The excitation power was set to 1 mW to prevent thermal damage of the graphene. Hall-effect measurements of graphene on various substrates were performed using the van-der-Pauw geometry with a sheet size of 1 cm^2. Solar cell characterization was performed under simulated AM1.5G sun light that was calibrated using an ISE certified Si reference diode. The active area of the perovskite solar cells was 0.16 cm^2 in case of Au electrodes and 1.03 cm^2 in case of graphene electrodes. The latter ones were measured with an aperture of 0.16 cm^2, excluding the Au grid finger. In consideration to the known current hysteresis of perovskite solar cells [21,22] all current voltage J(V) measurements were taken in forward and reverse directions, using a delay time of 40 ms, an acquisition time of 20 ms and a step size of 0.01 V. The scan speed therefore was 0.167 V/s.. Defined pre-conditioning or light soaking was not performed prior to J(V) measurements, although known to improve device efficiency within several minutes [21]. Measurements were performed in air. Sample temperature was not controlled during measurement. The external quantum efficiency was measured without bias illumination and without any applied bias voltage. Diffuse transmission and reflection were measured using an integrating sphere with a Perkin Elmer spectrometer, calibrated from an ISE certified white standard.

3 Results and discussion

3.1 Graphene on organic layers Figure 2 shows the Raman spectra of graphene transferred onto a glass substrate using the modified transfer process. We chose to perform the Raman measurements on glass rather than on the complete cell stack, since organic materials like spiro-OMeTAD and the polymer support contain a large amount of carbon bonds that have vibrational modes close to 1600 cm^{-1} that overlap with the G mode of graphene.

The Raman spectrum of graphene on glass shows the characteristic Brillouin zone-center G mode and the double resonance 2D mode at 1588 and 2698 cm^{-1}, respectively. Grain boundaries and transfer related defects like wrinkles and cracks induce a small amount of intervalley scattering between neighbouring Dirac cones. This activates an additional resonance at 1352 cm^{-1}, which is known as the D mode. However, the concentration of defects is low, hence intervalley scattering resulting in the D' resonance at about 1620 cm^{-1} is not detected [23].

The line width of the 2D mode is sensitive to the number and stacking of graphene layers. In our samples the 2D resonance is purely Lorentzian type and its width amounts to 36 cm^{-1} FWHM, which indicates scattering at single-layered material [24]. However, bilayer turbostratic graphene may resemble the same 2D line width if the individual graphene sheets are rotated by angles larger than 15° [25]. Hence, we performed additional optical absorption measurements (not shown here) confirming the single layer absorption of 2.4 % at 550 nm.

For single layer graphene the charge carrier concentration influences the 2D/G intensity ratio and the G mode resonance frequency [26]. From the Raman data in Fig. 2, we obtain a 2D/G ratio of 3.5. Together with the G mode position this indicates a hole concentration in the low 10^{12} cm^{-2} regime, which is corroborated using Hall Effect measurements.

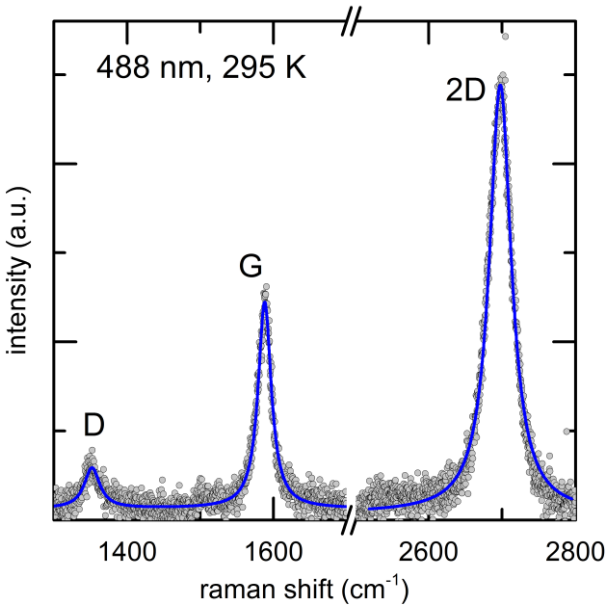

Figure 2 Baseline corrected Raman spectra of a graphene layer measured at a temperature of 295 K (circles). The blue line depicts a Lorentzian fit of the D, G, and 2D resonances. The excitation wavelength was λ = 488 nm. The Raman spectra were taken on graphene on a glass substrate using an identical transfer process as applied for graphene on organic layers.

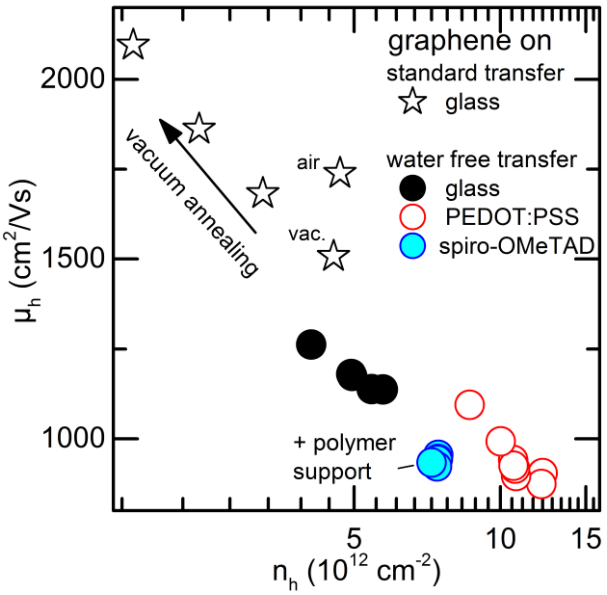

Figure 3 Hole mobility and charge carrier density of graphene layers on various substrates as obtained from Hall-effect measurements. The size of the specimens amounted to 1 cm^2. Stars depict data of graphene on glass using transfer from aqueous solution, while circles denote the used water free transfer. Filled black circles denote graphene on glass, open red circles: graphene on glass/PEDOT:PSS, filled blue circles: graphene on glass/spiro-OMeTAD. Measurements were performed first at room temperature in air and vacuum and second at elevated temperatures (vacuum annealing). In case of spiro-OMeTAD the maximal temperature was 55°C, being well below the glass temperature of spiro-OMeTAD [30].

The influence of underlying organic layers and the different transfer techniques on the electrical properties of graphene is investigated on dedicated 1 cm^2 sized samples for Hall-effect measurements. Figure 3 summarizes the measured charge carrier mobility μ versus the charge carrier density n of graphene. It has to be noted that holes are the majority charge carriers for all measured samples. This p-type character is in agreement with the previously identified 2D/G ratio [26].

Following a transfer from aqueous solution [18,27] of graphene on glass (open stars) results in a moderate charge carrier density, n_h, of around $4.6*10^{12}$ cm^{-2} and a high mobility, μ_h, of 1739 cm^2/Vs and 1507 cm^2/Vs, as measured in air and vacuum respectively. Moderate annealing to 100°C under vacuum allows the removal of adsorbents. Such adsorbents, originating from the atmosphere or as process residuals (e.g. O_2, H_2O, Cl^- ….), are known to alter the electrical properties of graphene via field effect doping [28,29]. As result of the adsorbent removal, charge carrier density reduces almost by a factor of three, while at the same time mobility increases well above 2000 cm^2/Vs. Naturally this affects the graphene sheet resistance, as calculated from equation 1.

$$R_{sq}^{graphene} = \frac{1}{n_h \cdot e \cdot \mu_h} \quad (1)$$

Hereby e denotes the electron's elementary charge of 1.60×10^{-19} C. In the present case, the graphene sheet resistance increases by a factor of two.

A water free transfer, as of course needed for the implementation of graphene in perovskite solar cells [31], alters nature and amount of adsorbents. In the present case (filled black circles), field effect doping increases the hole density to $5.7*10^{12}$ cm, while scattering at defects reduces the mobility to around 1200 cm^2/Vs.

Most important for the implementation in perovskite solar cells however is the effect of underlying organic thin films. PEDOT:PSS depicted as red open circles in figure 3 efficiently increases the hole density in graphene by more than 100 % to $1.2*10^{13}$ cm^{-2}. Consequently, the sheet resistance decreases by about 50 %, as compared to an identical transferred graphene layer on glass. Such field effect doping of PEDOT:PSS has been reported recently [17]. Although PEDOT:PSS may serve as efficient hole transporting material in inverted perovskite solar cells as bottom cathode [32–34], the regular architecture (top cathode) requires orthogonal solvents, such as chlorobenzene. Typically small molecules such as spiro-OMeTAD, dissolved in chlorobenzene enable optimal processability and performance [30,35]. Most remarkably Hall-effect measurements on spiro-OMeTAD/graphene (blue circles) reveal an efficient field effect doping, too. The hole density is increased by 30 % to $7.45*10^{12}$ cm^{-2}. Furthermore a highly transparent polymer cap proved to efficiently stabilize ad-

sorbent field effect doping, which elsewise is removed over time or during vacuum annealing. The combined effects lower the graphene sheet resistance by 24 %, compared to bare glass samples. However, the influence of spiro-OMeTAD additives, such as LiTFSI and TBP, on graphene field effect doping is still under investigation.

3.2 Solar cell performance Based on the gained knowledge on the mutual impact of graphene on organic thin films large area graphene was implemented in perovskite solar cells. Figure 4 presents the obtained current voltage *J*(V) characteristics of graphene (or Au) contacts on $CH_3NH_3PbI_3$ and $CH_3NH_3PbI_3$/spiro-OMeTAD. All solar cells showed hysteresis depending on the voltage sweep direction, as indicated by arrows in figure 4. The effect is reported to be especially severe in the present case of a planar $TiO_2/CH_3NH_3PbI_3$ interface, most probably due to imbalanced charge collection. [21,22] The effect may be mitigated inserting a thin PCBM layer at the $TiO_2/CH_3NH_3PbI_3$ interface. [36] In order to focus on the variation of the top contact, it is sufficient to discuss results obtained from the reverse *J*(V) scan, bold symbols in figure 4. . Table 1 shows the derived solar cell parameters. In all cases a polymer cap is used to stabilize additional adsorbent doping. The sheet resistivity of the used graphene batch was estimated to 350 Ω/sq as measured on glass by use of transfer from aqueous solution.

The green crosses in figure 4, depict results for graphene implemented on bare $CH_3NH_3PbI_3$. The *J*(V) curve in general represents a poor diode behaviour. The open circuit voltage (V_{OC}) amounts to 60 mV only. In contrast *J*(V) curves measured for $CH_3NH_3PbI_3$/Au, as processed on the same substrate follow nicely expected diode behaviour with a V_{OC} of 450 mV. It seems likely that the $CH_3NH_3PbI_3$/graphene interface is highly defective and therefore allowing severe recombination processes. This may explain the observed resistive behaviour. Sophisticated surface passivation, e.g. via supra-molecular halogen bonds [37] is needed for future developments. As remark, V_{OC} values of up to 0.7 V have been reported for optimized solar cells based on $TiO_2/CH_3NH_3PbI_3$/Au [38].

Figure 4, red squares presents *J*(V) characteristics of $CH_3NH_3PbI_3$/spiro-OMeTAD/graphene. Again 80 nm of Au on $CH_3NH_3PbI_3$/spiro-OMeTAD (black dots) serve as non-transparent reference, processed on the same substrate. First of all, both *J*(V) curves showed diode behaviour with fill factors (FF) above 50 %. Therefore, interface defects between $CH_3NH_3PbI_3$/spiro-OMeTAD and spiro-OMeTAD/graphene seem to be tolerable or non-present. The V_{OC} of the transparent graphene contacted solar cell amounts to 950 mV, which is close to the obtained 1 V for Au contacts. Analysis of 38 identically processed reference cells revealed a mean value (0.99±0.04) V for the V_{OC} with Au contacts. Therefore, the implementation of graphene as highly transparent contact was successful providing that spiro-OMeTAD ensures proper surface passivation and hole selectivity. Nevertheless, the short circuit current density, J_{SC}, of the $CH_3NH_3PbI_3$/spiro-OMeTAD/ graphene device is reduced to about 12 mA/cm^2. As proven later, this is an issue of insufficient absorber thickness only. Still the transparent graphene contact allowed a respectable power conversion efficiency of 6.02 % under AM1.5 conditions. The non-transparent Au reference in comparison showed 10.2 % on the same substrate (mean value (10.3±1.3) %). As remark higher absorber quality with fewer pinholes (compare figure 1) as e.g. obtained by evaporation easily allows high efficiency in the same planar configuration. [39]

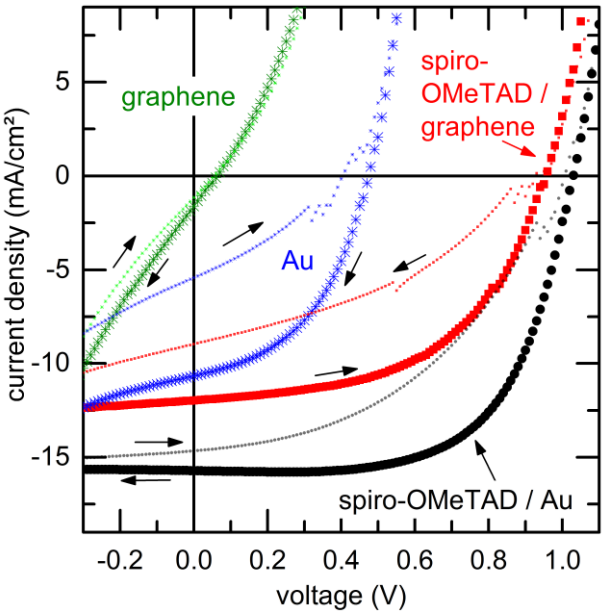

Figure 4 Current-voltage characteristics of perovskite solar cells with various transparent contacts, and as reference a standard non transparent contact consisting of 80 nm Au. Green crosses depict data for $CH_3NH_3PbI_3$/graphene, blue crosses for $CH_3NH_3PbI_3$/Au. Red squares show data for $CH_3NH_3PbI_3$/spiro-OMeTAD/graphene and black circles for $CH_3NH_3PbI_3$/spiro-OMeTAD/Au. Scan speed of the current voltage scan was 0.167 V/s. In respect to known hysteresis forward and backward scans are indicated by arrows. The active area of the device was either defined using a 4x4 mm^2 mask or a 4x4 mm^2 contact.

Table 1 Summarized solar cell parameters for various top contacts on $CH_3NH_3PbI_3$.

hole contact type	V_{OC} (V)	J_{SC} (mA/cm^2)	FF (%)	η (%)
Spiro-OMeTAD /Au	1.03	-15.75	62.9	10.2
Spiro-OMeTAD /graphene	0.95	-11.97	52.7	6.02
graphene	0.06	-1.60	23.1	0.02
Au	0.47	-10.67	45.8	2.3

3.3 Charge collection & transparency of spiro-OMeTAD/graphene vs. Au Defect free implementation and identical charge collection efficiency is concluded from identical open circuit voltages, as shown before. The statement is substantiated measuring the external quantum efficiency of identically prepared devices. Figure 5a shows external- (EQE) and internal-quantum efficiency (IQE) of perovskite solar cells with spiro-OMeTAD/graphene and spiro-OMeTAD/Au contacts, respectively. The IQE was calculated from diffuse reflection and transmission measurements according to equation (2).

$$IQE(\lambda) = \frac{EQE(\lambda)}{1-R(\lambda)-T(\lambda)} \quad (2)$$

The IQE is identical for both graphene and Au contacts, depicted as red and black dashed lines. The IQE maxima amount to 77.3 % and 76.1 % for graphene and Au respectively. Supplementary optical simulations (not shown) explain the slightly larger IQE for graphene between 500 and 700 nm. In this spectral regime Au causes considerable parasitic absorption. Despite observed identical IQE, single pass absorption reduces the EQE between 500 and 800 nm for graphene compared to Au, red and black solid lines. Measured EQE integrates to a short circuit current density of 13.4 and 15.1 mA/cm^2 for graphene and Au respectively.

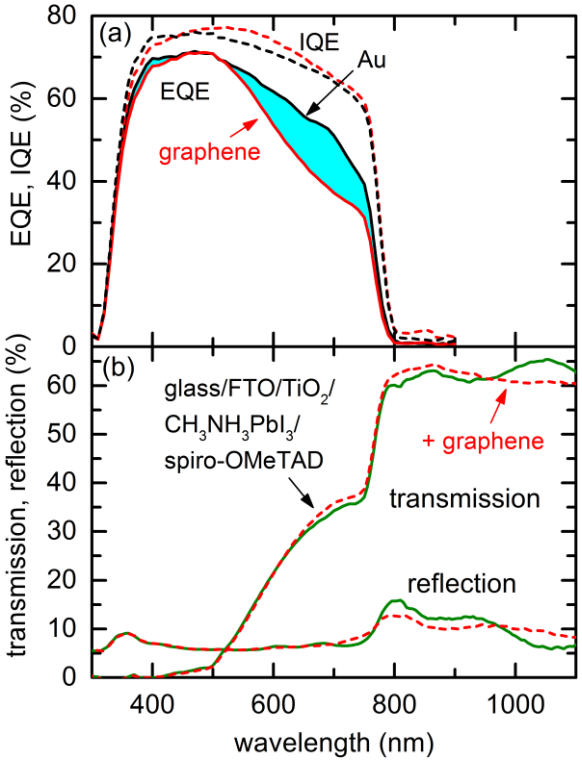

Figure 5 (a) External (EQE) and internal (IQE) quantum efficiency of graphene and Au contacted perovskite solar cells depicted as red solid/dashed and black solid/dashed lines respectively. (b) Diffuse transmission and reflection of glass/FTO/$CH_3NH_3PbI_3$/spiro-OMeTAD with and without graphene/polymer support depicted as solid olive and dotted red curves.

As outlined before the intention of introducing a transparent graphene based contact is the realisation of perovskite/silicon tandem solar cells. Therefore figure 5b shows diffuse reflection and transmission of perovskite solar cells with and without spiro-OMeTAD/graphene. In general, the transmission of the glass/FTO/TiO_2/ $CH_3NH_3PbI_3$/spiro-OMeTAD layer stack is dominated by parasitic absorption within used glass/FTO for $\lambda > 800$ nm. Absorption of about 30 % within glass/FTO (not shown) decreases the sub-band gap transmission of the complete device to about 60 %. The application of the graphene/polymer contact introduced minor parasitic absorption. At the same time the graphene/polymer layer served as anti-reflection coating (see fig. 5b, green solid and dashed red lines). This improved transmission of the glass/FTO/TiO_2/$CH_3NH_3PbI_3$/ spiro-OMeTAD/graphene/ polymer stack, of about 64 % above 800 nm can be efficiently used in silicon bottom solar cells, as presented in [11].

3.5 Perspective on graphene top contacts for perovskite and monolithic perovskite/Si tandem solar cells Using gently transferred graphene layers as transparent contacts for perovskite solar cells has several advantages. First, there is no deterioration of perovskite and its organic layers, such as spiro-OMeTAD. This allows to achieve identical open circuit voltages and internal quantum efficiencies as compared to Au. Furthermore implementation of graphene is compatible to solution processing and future roll to roll processing. At the same time an anti-reflection coating is implemented. However disadvantages such as limited sheet resistance have to be discussed for a realistic potential assessment.

As observed in figure 4, high sheet resistance of large area graphene contacts affects solar cell performance by a slight reduction in fill factor from 63 % on Au (1.63 Ω/sq) to 53 %. Such resistive losses can be minimized using multiple graphene layers and/or additional metal grids. The latter is common practice for typical commercially available solar cells. Figure 6 illustrates the minimization process by depicting the graphene top contact series resistance as a function of graphene sheet resistance $R_{graphene}$ and grid spacing. Calculation is performed for a standard metal grid, according to equation (3) [40]. Any contribution of grid finger resistance is reasonably neglected.

$$R_S = R_{graphene} \cdot \frac{a^2}{12} \quad (3)$$

Estimation of the tolerable series resistance is performed according to equation (4) [40].

$$R_S^{tolerable} < \frac{1}{100} \cdot \frac{V_{OC}}{J_{SC}} \quad (4)$$

The tolerable series resistance of a typical perovskite single junction with a V_{OC} of 1 V and a J_{SC} of 15 mA/cm^2

amounts to 0.6 Ωcm, depicted as solid yellow line in fig. 6. Optimal grid spacing therefore varies between 0.35 and 0.16 cm, depending on the number of stacked graphene layers. Large area-graphene, as used in this work, with and without field effect doping by spiro-OMeTAD was of course far from optimum.

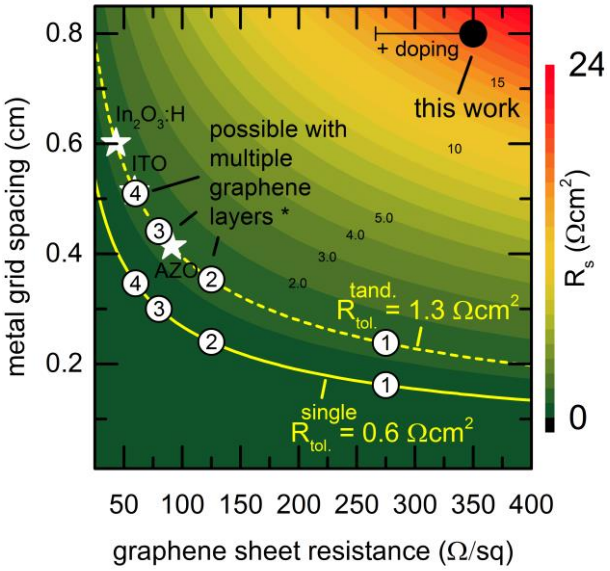

Figure 6 Contour plot of the series resistance, R_S, of the spiro-OMeTAD/graphene top contact as function of the graphene sheet resistance and the metal grid spacing. Tolerable series resistance of representative perovskite single and monolithic perovskite/silicon tandem cells are plotted as yellow solid and dashed lines. The black circle denotes the graphene sheet resistance and grid spacing as used in this work. Open circles denote a realistic estimation of the needed grid spacing for a desired number of graphene layers. Used sheet resistance values [41], $R_{graphene}$, hereby are compatible with large area graphene and roll to toll processing. Stars denote sheet resistance and grid spacing for typical TCO's with 80 nm thickness.

Monolithic perovskite/silicon tandem solar cells on the other hand should allow for V_{OC} values close to the sum of the individual single junctions, while halving the short circuit current. As presented by Albrecht et al. [13], V_{OC} values of 1.785 V with an J_{SC} of 14 mA/cm^2 are possible. This weakens the condition for the tolerable series resistance to around 1.3 Ωcm. Optimal grid spacing therefore varies between 0.51 and 0.24 cm only, depending on the number of stacked graphene layers. Assuming a grid finger thickness of 50 µm [42], such grids should induce shading losses well below 1 and 2 %. At this point we have to note that the absorption of graphene layer stacks amounts to 2.6, 4.9, 7.1 and 9.9 % at 550 nm for 1, 2, 3 and 4 layers, respectively. [41]

As comparison to graphene based contacts, black stars denote typical transparent conductive oxides (TCO's). Optimized TCO's, such as aluminium doped zinc oxide (AZO), indium toped tin oxide (ITO) and hydrogen doped indium oxides (In_2O_3:H) provide specific resistance values of up to 728, 472 and 345 µΩcm, respectively [43]. A reasonable TCO thickness of 80 nm, supressing first order interference, leads to sheet resistance values of 91, 59 and 43 Ω/sq, respectively.

Fig. 6 illustrated design rules for the implementation of spiro-OMeTAD/graphene in perovskite solar cells. If combined with a metal grid of around 5 mm pitch, the developed contact system is an excellent alternative to conventional TCO's. Further low absorption in both the VIS and IR regime as well as the gentle and defect free implementation renders them as excellent solution for monolithic perovskite/silicon tandem solar cells. High tolerable series resistances as well as in-situ graphene doping should facilitate future implementation and optimization.

4 Conclusion In summary, conducted experiments revealed mutual impacts of graphene on perovskite solar cells and their organic layers. The direct implementation of graphene on $CH_3NH_3PbI_3$ is limited by a highly defective interface. Insertion of spiro-OMeTAD allows successful implementation of transparent graphene monolayers. Characterised devices show similar open circuit voltages of around 1 V and identical charge collection efficiencies above 77 %. The manifold role of spiro-OMeTAD, interface passivation, hole selectivity & graphene doping is revealed. Dedicated Hall-effect measurements proved an 30 % increase in hole density by field effect doping through pristine spiro-OMeTAD. Additional adsorbent doping of 22 % could be stabilized using a polymer cap. The developed strategy comprising of the combined route of spiro-OMeTAD and stabilized adsorbent doping, lowered the graphene sheet resistance by 24 %. This is a first step towards the targeted application in high performance monolithic perovskite/silicon tandem solar cells

Acknowledgements The authors thank Tobias Hänel and Karolina Mack from the Competence Center Thin-film- and Nanotechnology for Photovoltaics Berlin (PVcomB) for support in EQE and UV/VIS measurements. The authors are grateful to Carola Klimm for taking SEM micrographs. B. Hase is acknowledged for experiments on sputtered ITO contacts. Rodrigo Sáez from the institute for heterogeneous materials systems is acknowledged for support in TiO_2 spray pyrolysis. Financial support from the Helmholtz Energy Alliance (Hybrid Photovoltaic), the European Union Seventh Framework programme (grant. No. 604032) and the DFG priority program (SPP 1459) are gratefully acknowledged.

References

[1] G. Xing, N. Mathews, S.S. Lim, N. Yantara, X. Liu, D. Sabba, M. Grätzel, S. Mhaisalkar, T.C. Sum, Nat. Mater. **13**, 476 (2014).

[2] K. Zhu, T. Miyasaka, J.Y. Kim, I. Mora-Seró, J. Phys. Chem. Lett. **6**, 2315 (2015).

[3] S.D. Stranks, G.E. Eperon, G. Grancini, C. Menelaou,

M.J.P. Alcocer, T. Leijtens, L.M. Herz, A. Petrozza, H.J. Snaith, Science. **342**, 341 (2013).

[4] C. Wehrenfennig, G.E. Eperon, M.B. Johnston, H.J. Snaith, L.M. Herz, Adv. Mater. **26**, 1584 (2014).

[5] W. Tress, N. Marinova, O. Inganäs, M.K. Nazeeruddin, S.M. Zakeeruddin, M. Graetzel, Adv. Energy Mater. **5**, 1400812 (2015).

[6] N.J. Jeon, J.H. Noh, W.S. Yang, Y.C. Kim, S. Ryu, J. Seo, S. Il Seok, Nature. **517**, 476 (2015).

[7] J.H. Noh, S.H. Im, J.H. Heo, T.N. Mandal, S. Il Seok, Nano Lett. **13**, 1764 (2013).

[8] W.S. Yang, J.H. Noh, N.J. Jeon, Y.C. Kim, S. Ryu, J. Seo, S.I. Seok, Science. **348**, 1234 (2015).

[9] G.E. Eperon, S.D. Stranks, C. Menelaou, M.B. Johnston, L.M. Herz, H.J. Snaith, Energy Environ. Sci. **7**, 982 (2014).

[10] H. Uzu, M. Ichikawa, M. Hino, K. Nakano, T. Meguro, J.L. Hernández, H.-S. Kim, N.-G. Park, K. Yamamoto, Appl. Phys. Lett. **106**, 013506 (2015).

[11] F. Lang, M.A. Gluba, S. Albrecht, J. Rappich, L. Korte, B. Rech, N.H. Nickel, J. Phys. Chem. Lett. **6**, 2745 (2015).

[12] P. Löper, S.-J. Moon, S. Martín de Nicolas, B. Niesen, M. Ledinsky, S. Nicolay, J. Bailat, J.-H. Yum, S. De Wolf, C. Ballif, Phys. Chem. Chem. Phys. **17**, 1619 (2015).

[13] S. Albrecht, M. Saliba, J.P. Correa Baena, F. Lang, L. Kegelmann, M. Mews, L. Steier, A. Abate, J. Rappich, L. Korte, R. Schlatmann, M.K. Nazeeruddin, A. Hagfeldt, M. Grätzel, B. Rech, Energy Environ. Sci. **9**, 81 (2016).

[14] J. Werner, G. Dubuis, A. Walter, P. Löper, S.-J. Moon, S. Nicolay, M. Morales-Masis, S. De Wolf, B. Niesen, C. Ballif, Sol. Energy Mater. Sol. Cells. **141**, 407 (2015).

[15] L. Kranz, A. Abate, T. Feurer, F. Fu, E. Avancini, J. Löckinger, P. Reinhard, S.M. Zakeeruddin, M. Grätzel, S. Buecheler, A.N. Tiwari, J. Phys. Chem. Lett. **6**, 2676 (2015).

[16] V.V. Brus, M.A. Gluba, X. Zhang, K. Hinrichs, J. Rappich, N.H. Nickel, Phys. Status Solidi. **211**, 843 (2014).

[17] P. You, Z. Liu, Q. Tai, S. Liu, F. Yan, Adv. Mater. **27**, 3632 (2015).

[18] M.A. Gluba, D. Amkreutz, G. V. Troppenz, J. Rappich, N.H. Nickel, Appl. Phys. Lett. **103**, 073102 (2013).

[19] X. Li, W. Cai, J. An, S. Kim, J. Nah, D. Yang, R. Piner, A. Velamakanni, I. Jung, E. Tutuc, S.K. Banerjee, L. Colombo, R.S. Ruoff, Science. **324**, 1312 (2009).

[20] T. Baikie, Y. Fang, J.M. Kadro, M. Schreyer, F. Wei, S.G. Mhaisalkar, M. Graetzel, T.J. White, J. Mater. Chem. A. **1**, 5628 (2013).

[21] E.L. Unger, E.T. Hoke, C.D. Bailie, W.H. Nguyen, A.R. Bowring, T. Heumuller, M.G. Christoforo, M.D. McGehee, Energy Environ. Sci. **7**, 3690 (2014).

[22] H.J. Snaith, A. Abate, J.M. Ball, G.E. Eperon, T. Leijtens, N.K. Noel, S.D. Stranks, J.T.-W. Wang, K. Wojciechowski, W. Zhang, J. Phys. Chem. Lett. **5**, 1511 (2014).

[23] A.C. Ferrari, D.M. Basko, Nat. Nanotechnol. **8**, 235 (2013).

[24] M.A. Pimenta, G. Dresselhaus, M.S. Dresselhaus, L.G. Cançado, A. Jorio, R. Saito, Phys. Chem. Chem. Phys. **9**, 1276 (2007).

[25] R. He, T.F. Chung, C. Delaney, C. Keiser, L.A. Jauregui, P.M. Shand, C.C. Chancey, Y. Wang, J. Bao, Y.P. Chen, Nano Lett. **13**, 3594 (2013).

[26] A. Das, S. Pisana, B. Chakraborty, S. Piscanec, S.K. Saha, U. V Waghmare, K.S. Novoselov, H.R. Krishnamurthy, A.K. Geim, A.C. Ferrari, A.K. Sood, Nat. Nanotechnol. **3**, 210 (2008).

[27] G.V. Troppenz, M.A. Gluba, M. Kraft, J. Rappich, N.H. Nickel, J. Appl. Phys. **114**, 214312 (2013).

[28] H. Liu, Y. Liu, D. Zhu, J. Mater. Chem. **21**, 3335 (2011).

[29] T.O. Wehling, M.I. Katsnelson, A.I. Lichtenstein, Chem. Phys. Lett. **476**, 125 (2009).

[30] T. Malinauskas, D. Tomkute-Luksiene, R. Sens, M. Daskeviciene, R. Send, H. Wonneberger, V. Jankauskas, I. Bruder, V. Getautis, ACS Appl. Mater. Interfaces. **7**, 11107 (2015).

[31] J. Yang, B.D. Siempelkamp, D. Liu, T.L. Kelly, ACS Nano. **9**, 1955 (2015).

[32] C. Roldán-Carmona, O. Malinkiewicz, A. Soriano, G. Mínguez Espallargas, A. Garcia, P. Reinecke, T. Kroyer, M.I. Dar, M.K. Nazeeruddin, H.J. Bolink, Energy Environ. Sci. **7**, 994 (2014).

[33] X. Bao, Q. Zhu, M. Qiu, A. Yang, Y. Wang, D. Zhu, J. Wang, R. Yang, J. Mater. Chem. A. **3**, 19294 (2015).

[34] D. Forgács, M. Sessolo, H.J. Bolink, J. Mater. Chem. A. **3**, 14121 (2015).

[35] J.P. Correa Baena, L. Steier, W. Tress, M. Saliba, S. Neutzner, T. Matsui, F. Giordano, T.J. Jacobsson, A.R. Srimath Kandada, S.M. Zakeeruddin, A. Petrozza, A. Abate, M.K. Nazeeruddin, M. Grätzel, A. Hagfeldt, Energy Environ. Sci. **8**, 2928 (2015).

[36] A.H. Ip, L.N. Quan, M.M. Adachi, J.J. McDowell, J. Xu, D.H. Kim, E.H. Sargent, Appl. Phys. Lett. **106**, 143902 (2015).

[37] A. Abate, M. Saliba, D.J. Hollman, S.D. Stranks, K. Wojciechowski, R. Avolio, G. Grancini, A. Petrozza, H.J. Snaith, Nano Lett. **14**, 3247 (2014).

[38] S. Aharon, B. El Cohen, L. Etgar, J. Phys. Chem. C. **118**, 17160 (2014).

[39] M. Liu, M.B. Johnston, H.J. Snaith, Nature. **501**, 395 (2013).

[40] T. Dittrich, Materials Concepts for Solar Cells, 1st ed., Imperial College Press, London, 2014.

[41] S. Bae, H. Kim, Y. Lee, X. Xu, J.-S. Park, Y. Zheng, J. Balakrishnan, T. Lei, H.R. Kim, Y. Il Song, Y.-J. Kim, K.S. Kim, B. Ozyilmaz, J.-H. Ahn, B.H. Hong, S. Iijima, Nat. Nanotechnol. **5**, 574 (2010).

[42] T. Dullweber, S. Gatz, H. Hannebauer, T. Falcon, R. Hesse, J. Schmidt, R. Brendel, Prog. Photovoltaics Res. Appl. **20**, 630 (2012).

[43] H. Scherg-Kurmes, S. Körner, S. Ring, M. Klaus, L. Korte, F. Ruske, R. Schlatmann, B. Rech, B. Szyszka, Thin Solid Films. **594**, 316 (2015).